Journal of Computational Physics 228 (2009) 8807–8829

Contents lists available at ScienceDirect

Journal of Computational Physics

journal homepage: www.elsevier.com/locate/jcp

An efficient fluid–solid coupling algorithm for single-phase flows

Yen Ting Ng [a], Chohong Min [b,*], Frédéric Gibou [a,c]

[a] Computer Science Department, University of California, Santa Barbara, CA 93106, United States
[b] Mathematics Department and Research Institute for Basic Sciences, KyungHee University, Seoul 130-701, Republic of Korea
[c] Mechanical Engineering Department, University of California, Santa Barbara, CA 93106, United States

ARTICLE INFO

Article history:
Received 19 May 2009
Received in revised form 21 August 2009
Accepted 27 August 2009
Available online 13 September 2009

Keywords:
Navier–Stokes equations
Solid–fluid interaction
Irregular domain
Hodge decomposition

ABSTRACT

We present a simple and efficient fluid–solid coupling method in two and three spatial dimensions. In particular, we consider the numerical approximation of the Navier–Stokes equations on irregular domains and propose a novel approach for solving the Hodge projection step on arbitrary shaped domains. This method is straightforward to implement and leads to a symmetric positive definite linear system for both the projection step and for the implicit treatment of the viscosity. We demonstrate the accuracy of our method in the L^1 and L^∞ norms and present its removing the errors associated with the conventional rasterization-type discretizations. We apply this method to the simulation of a flow past a cylinder in two spatial dimensions and show that our method can reproduce the known stable and unstable regimes as well as correct lift and drag forces. We also apply this method to the simulation of a flow past a sphere in three spatial dimensions at low and moderate Reynolds number to reproduce the known steady axisymmetric and non-axisymmetric flow regimes. We further apply this algorithm to the coupling of flows with moving rigid bodies.

1. Introduction

The Navier–Stokes equations are the fundamental equations of fluid dynamics with countless applications, from engineering to biology. More often than not, it is necessary to simulate fluid flows on irregular domains and to compute accurately the velocity field near the solids' boundary. A typical example is the computation of the lift and drag forces on irregular geometries, which requires the integration of the velocity field around the objects' boundary. Another field that requires accurate computations of the velocity field near objects' wall is porous media flows: the interaction between the fluid and the solid is specific to the physical characteristics of the solid, e.g. through the definition of the so-called contact angle. This condition can be imposed through the so-called Navier-slip condition, which in turn requires the accurate computation of the fluid velocity adjacent to the solids' boundary. We note that the notion of contact angles only makes sense in the context of two-phase flows and might involve other issues than the accurate solution of the fluid velocity near the object boundary. Nevertheless, it emphasizes that it is important to develop simple and accurate Navier–Stokes solvers on irregular domains that guarantee the convergence of the velocity field near the objects' boundary.

The projection method, introduced by Chorin [6], is a very efficient method to solve the Navier–Stokes equations. Its ease of implementation on regular domains is based on the fact that the discretization of the Poisson equation can be decoupled in each of the Cartesian directions, so that imposing the necessary Neumann boundary condition is straightforward. This is not at all the case for arbitrary geometries. The difficulty in using a projection method on irregular domains is thus primarily

* Corresponding author.
E-mail address: chohong@khu.ac.kr (C. Min).

0021-9991/$ - see front matter © 2009 Elsevier Inc. All rights reserved.
doi:10.1016/j.jcp.2009.08.032

to impose the Neumann boundary condition when the contour of the solid objects is not necessarily aligned with the Cartesian grids. Several approaches such as the immersed boundary method of Peskin [21], the immersed interface method LeVeque and Li [14] and the ALE method of Hirt [10] have been proposed to represent the boundary of an object and simulate its influence on the fluid dynamics, often with the side-effects of being more computationally expensive or being more challenging to implement. Finite element methods produce accurate results but the need to conform elements to the objects' boundary is less attractive than a pure Eulerian approach.

Due to the lack of a simple method that can accurately solve this problem, one often opts for describing the solid boundary by rasterization, i.e. the objects are approximated by forcing their boundary to follow the grid lines. This approach is obviously straightforward to implement, but it produces solutions that do not converge in the L^∞ norm and show staircase effects near the walls; only the average velocity field is convergent. This loss of accuracy can obviously be problematic for the practical problems mentioned above. In [2], Batty et al. presented a methodology based on energy minimization to account for the fluid–solid coupling. This method is Eulerian and is able to reproduce the average fluid dynamics and considers boundary that are not necessarily aligned with the grid lines. However, as we show in Section 4, this method is not convergent in the L^∞ norm with large $O(1)$ errors near the solid boundary. In this paper, we present a novel discretization that is straightforward to implement, produces a symmetric positive definite linear system and is second-order accurate in both the L^1 and L^∞ norms in two spatial dimensions, and first-order accurate in both norms in three spatial dimensions.

2. Standard projection method

The incompressible Navier–Stokes equations for the motion of Newtonian fluids are written as:

$$\rho(\mathbf{U}_t + (\mathbf{U}\cdot\nabla)\mathbf{U}) = -\nabla p + \mu\Delta\mathbf{U} + \rho\mathbf{F},$$
$$\nabla\cdot\mathbf{U} = 0,$$

where t is time, ρ the fluid density, $\mathbf{U} = \langle u, v, w\rangle$ the velocity field, p the pressure, μ the constant viscosity and $\mathbf{F}$ describes external forces such as the gravity field.

The seminal work of Chorin [6] described a method to solve the Navier–Stokes equations based on the Hodge decomposition, which states that any vector field $\mathbf{U}^*$ can be decomposed into the sum of a divergence-free vector field $\mathbf{U}$ and a weighted gradient field $\frac{\nabla p}{\rho}$ for some scalar function p and some known positive function ρ. The projection method consists of three stages. First, given the velocity field $\mathbf{U}^n$ at time $t^n = n\Delta t$, an intermediate velocity $\mathbf{U}^*$ is calculated for a time step Δt by ignoring the pressure component, e.g.:

$$\frac{\mathbf{U}^* - \mathbf{U}^n}{\Delta t} + \mathbf{U}^n\cdot\nabla\mathbf{U}^n = \frac{\mu^n}{\rho^n}\Delta\mathbf{U}^n + \mathbf{F}$$

in the case of a simple Euler step in time. Next, the incompressibility condition $\nabla\cdot\mathbf{U}^{n+1} = 0$ for the new fluid velocity is enforced by choosing the (scalar function) pressure p^{n+1} to satisfy the Poisson equation:

$$\nabla\cdot\left(\frac{\nabla p^{n+1}}{\rho^{n+1}}\right) = \frac{\nabla\cdot\mathbf{U}^*}{\Delta t} \tag{1}$$

with Neumann boundary conditions on the domain's boundaries and on the solid objects:

$$n\cdot\left(\frac{\nabla p}{\rho}\right) = n\cdot(\mathbf{U}^*_{bc} - \mathbf{U}_{bc}),$$

where $\mathbf{U}_{bc}$ is the imposed velocity field on the solid's boundary. Finally, the fluid velocity $\mathbf{U}^{n+1}$ at the new time step t^{n+1} is defined as a projection of $\mathbf{U}^*$ onto the divergence-free vector space:

$$\mathbf{U}^{n+1} = \mathbf{U}^* - \Delta t\frac{\nabla p^{n+1}}{\rho^{n+1}}.$$

3. A novel discretization of the projection method on irregular domains

In the case of an irregular domain, it is not obvious how to choose a scalar function p that will enforce the divergence free condition. The reason is due to the fact that it is not straightforward to solve the Poisson equation with Neumann boundary conditions at the boundary of an irregular domain, especially if one seeks to design a simple methodology that can be applied dimension by dimension. In what follows, we introduce a novel discretization that solves this problem. The method is straightforward to implement and produces a symmetric linear system that can be inverted efficiently. Without loss of generality, we present our approach in two spatial dimensions.

Consider a vector field $\mathbf{U}^*$ on a domain Ω separated into two disjoint subsets Ω^- and Ω^+ such that $\Omega = \Omega^-\cup\Omega^+$, and Γ is the interface between Ω^- and Ω^+. We seek to solve the Navier–Stokes equations on the simply connected irregular domain Ω^- only. Assume that the domain Ω is represented by a level function ϕ such that $\Omega^- = \{\vec{x} : \phi(\vec{x}) \leqslant 0\}, \Omega^+ = \{\vec{x} : \phi(\vec{x}) > 0\}$

and $\Gamma = \{\vec{x} : \phi(\vec{x}) = 0\}$. Consider a MAC grid configuration and a cell $C_{ij} = \left[i-\frac{1}{2}, i+\frac{1}{2}\right] \times \left[j-\frac{1}{2}, j+\frac{1}{2}\right]$ partially covered by the irregular domain, as depicted in Fig. 1. Taking a finite volume approach, i.e. integrating the left hand side of Eq. (1) over C_{ij} and evoking the divergence theorem, we obtain:

$$\int_{C_{ij}\cap\Omega^-} \nabla\cdot\left(\frac{\nabla p}{\rho}\right) dA = \int_{C_{ij}\cap\Omega^-} \nabla\cdot\mathbf{U}^* \, dl,$$

where dA and dl refer to the area and length differentials, respectively. Similarly, for the right hand side of Eq. (1), we write:

$$\int_{\partial(C_{ij}\cap\Omega^-)} n\cdot\left(\frac{\nabla p}{\rho}\right) dA = \int_{\partial(C_{ij}\cap\Omega^-)} n\cdot\mathbf{U}^* \, dl.$$

Since the boundary $\partial(C_{ij}\cap\Omega^-)$ has two components, the faces of the grid cell $\partial C_{ij}\cap\Omega^-$ and the interface with the irregular external boundary $C_{ij}\cap\Gamma$, we consider separately the contribution of the two components. On a face $\left(i-\frac{1}{2}\right)\times\left[j-\frac{1}{2}, j+\frac{1}{2}\right]$, the length fraction of the face covered by the irregular domain $\{x|\phi(x)\leqslant 0\}$ is linearly approximated as:

$$L_{i-\frac{1}{2}j} = \begin{cases} \Delta y \frac{\phi_{i-\frac{1}{2}j-\frac{1}{2}}}{\phi_{i-\frac{1}{2}j-\frac{1}{2}} - \phi_{i-\frac{1}{2}j+\frac{1}{2}}} & \text{if } \phi_{i-\frac{1}{2}j-\frac{1}{2}} < 0 \text{ and } \phi_{i-\frac{1}{2}j+\frac{1}{2}} > 0, \\ \Delta y \frac{\phi_{i-\frac{1}{2}j+\frac{1}{2}}}{\phi_{i-\frac{1}{2}j+\frac{1}{2}} - \phi_{i-\frac{1}{2}j-\frac{1}{2}}} & \text{if } \phi_{i-\frac{1}{2}j-\frac{1}{2}} > 0 \text{ and } \phi_{i-\frac{1}{2}j+\frac{1}{2}} < 0, \\ \Delta y & \text{if } \phi_{i-\frac{1}{2}j-\frac{1}{2}} < 0 \text{ and } \phi_{i-\frac{1}{2}j+\frac{1}{2}} < 0, \\ 0 & \text{if } \phi_{i-\frac{1}{2}j-\frac{1}{2}} > 0 \text{ and } \phi_{i-\frac{1}{2}j+\frac{1}{2}} > 0. \end{cases}$$

By approximating the boundary integral on the grid faces as the product of the length and the sampled value at the center, we obtain:

$$-\int_{\partial(C_{ij}\cap\Omega^-)} n\cdot\left(\frac{\nabla p}{\rho}\right) \simeq \frac{L_{i-\frac{1}{2}j}}{\rho_{i-\frac{1}{2}j}}\cdot\frac{p_{ij}-p_{i-1j}}{\Delta x} + \frac{L_{i+\frac{1}{2}j}}{\rho_{i+\frac{1}{2}j}}\cdot\frac{p_{ij}-p_{i+1j}}{\Delta x} + \frac{L_{ij-\frac{1}{2}}}{\rho_{ij-\frac{1}{2}}}\cdot\frac{p_{ij}-p_{ij-1}}{\Delta y} + \frac{L_{ij+\frac{1}{2}}}{\rho_{ij+\frac{1}{2}}}\cdot\frac{p_{ij}-p_{ij+1}}{\Delta y} - \int_{C_{ij}\cap\Gamma} n\cdot(\mathbf{U}^*_{bc}-\mathbf{U}_{bc}),$$

where $\int_{C_{ij}\cap\Gamma}$ is the integral over the interface with the irregular external boundary, approximated using the geometric integration of Min and Gibou [17]. Similarly, we obtain an approximation of boundary integral of $\nabla\cdot\mathbf{U}^*$ as:

$$-\int_{\partial(C_{ij}\cap\Omega^-)} n\cdot(\mathbf{U}^*) \simeq L_{i-\frac{1}{2}j}\cdot u^*_{i-\frac{1}{2}j} - L_{i+\frac{1}{2}j}\cdot u^*_{i+\frac{1}{2}j} + L_{ij-\frac{1}{2}}\cdot v^*_{ij-\frac{1}{2}} - L_{ij+\frac{1}{2}}\cdot v^*_{ij+\frac{1}{2}} - \int_{C_{ij}\cap\Gamma} n\cdot\mathbf{U}^*_{bc}.$$

Finally, combining the discretizations above, we obtain the following Poisson problem with Neumann boundary condition as the definition of the scalar function p used for projecting the intermediate velocity $\mathbf{U}^*$ onto the divergence-free vector field on irregular domains:

$$\begin{aligned} &\frac{L_{i-\frac{1}{2}j}}{\rho_{i-\frac{1}{2}j}}\cdot\frac{p_{ij}-p_{i-1j}}{\Delta x} + \frac{L_{i+\frac{1}{2}j}}{\rho_{i+\frac{1}{2}j}}\cdot\frac{p_{ij}-p_{i+1j}}{\Delta x} + \frac{L_{ij-\frac{1}{2}}}{\rho_{ij-\frac{1}{2}}}\cdot\frac{p_{ij}-p_{ij-1}}{\Delta y} + \frac{L_{ij+\frac{1}{2}}}{\rho_{ij+\frac{1}{2}}}\cdot\frac{p_{ij}-p_{ij+1}}{\Delta y} \\ &\quad = L_{i-\frac{1}{2}j}\cdot u^*_{i-\frac{1}{2}j} - L_{i+\frac{1}{2}j}\cdot u^*_{i+\frac{1}{2}j} + L_{ij-\frac{1}{2}}\cdot v^*_{ij-\frac{1}{2}} - L_{ij+\frac{1}{2}}\cdot v^*_{ij+\frac{1}{2}} - \int_{C_{ij}\cap\Gamma} n\cdot\mathbf{U}_{bc}. \end{aligned} \tag{2}$$

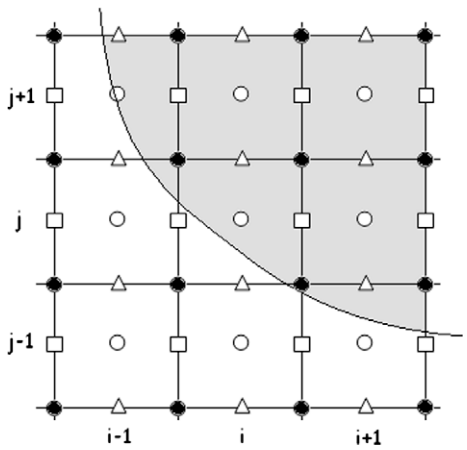

Fig. 1. Standard MAC grid configuration: the pressure is sampled at the cells' centers (circles), the x-component of the velocity field is sampled on the vertical faces (rectangles), and the y-component of the velocity field is sampled on the horizontal faces (triangles). The irregular domain is represented by the shaded area.

The above discretization forms a symmetric positive definite linear system for p (see Section 3.1) and obviously reduces to the standard linear system for regular domains. We also note that the linear system involves p at grid cells that are located outside and adjacent to the irregular domain, so the pressure at this location is solved for.

3.1. Symmetry positive definiteness of the linear system

The proof that the linear system is symmetric definite positive is trivial and a direct consequence of the fact that the length fractions $L_{i\pm\frac{1}{2},j\pm\frac{1}{2}}$ and densities $\rho_{i\pm\frac{1}{2},j\pm\frac{1}{2}}$ are located midway between grid nodes (at the flux locations as illustrated in Fig. 2) and the fact that their values are positive:

- For each grid node (i,j), Eq. (2) is used to fill one row $r=(j-1)N_x+i$ of the linear system, where N_x the number of nodes in the x-direction. The diagonal element $A_{r,r}$ of the linear system is given by

$$A_{r,r}=\frac{L_{i-\frac{1}{2},j}}{\Delta x\rho_{i-\frac{1}{2},j}}+\frac{L_{i+\frac{1}{2},j}}{\Delta x\rho_{i+\frac{1}{2},j}}+\frac{L_{i,j-\frac{1}{2}}}{\Delta y\rho_{i,j-\frac{1}{2}}}+\frac{L_{i,j+\frac{1}{2}}}{\Delta y\rho_{i,j+\frac{1}{2}}},$$

and the sum $\sum$ of the extra-diagonal elements is given by

$$\sum=-\frac{L_{i-\frac{1}{2},j}}{\Delta x\rho_{i-\frac{1}{2},j}}-\frac{L_{i+\frac{1}{2},j}}{\Delta x\rho_{i+\frac{1}{2},j}}-\frac{L_{i,j-\frac{1}{2}}}{\Delta y\rho_{i,j-\frac{1}{2}}}-\frac{L_{i,j+\frac{1}{2}}}{\Delta y\rho_{i,j+\frac{1}{2}}}.$$

Clearly the matrix is diagonally dominant, since $A_{r,r}+\sum=0$.

- The diagonal element $A_{r,r}$ is positive since the L's refer to (positive) length fractions, the ρ's refer to the (positive) fluid density and Δx and Δy are the (positive) grid spacing in the x- and y-directions, respectively.
- For a given row $r=(j-1)N_x+i$, the first extra-diagonal element to the right, $A_{r,r+1}$, is the coefficient in front of $p_{i+1,j}$, i.e. $\frac{L_{i+\frac{1}{2},j}}{\Delta x\rho_{i+\frac{1}{2},j}}$. Its corresponding symmetric element, $A_{r+1,r}$ is the coefficient of the first extra-diagonal element to the left of $A_{r+1,r+1}$, i.e. $\frac{L_{i-\frac{1}{2},j}}{\Delta x\rho_{i-\frac{1}{2},j}}$ with $i=i+1$, thus $\frac{L_{i+\frac{1}{2},j}}{\Delta x\rho_{i+\frac{1}{2},j}}$. Likewise, the second extra-diagonal element to the right, $A_{r,r+N_x}$, is the coefficient in front of $p_{i,j+1}$, i.e. $\frac{L_{ij+\frac{1}{2}}}{\Delta x\rho_{ij+\frac{1}{2}}}$. Its corresponding symmetric element, $A_{r+N_x,r}$ is the coefficient of the second extra-diagonal element to the left of $A_{r+N_x,r+N_x}$, i.e. $\frac{L_{ij-\frac{1}{2}}}{\Delta x\rho_{ij-\frac{1}{2}}}$ with $j=j+1$, thus $\frac{L_{ij+\frac{1}{2}}}{\Delta x\rho_{ij+\frac{1}{2}}}$. Therefore the linear system is symmetric.

The linear system is symmetric, diagonally dominant with positive diagonal elements. Therefore the linear system is symmetric definite positive.

3.2. Convergence of the new discretization

Consider an irregular domain $\Omega^-=\{(x,y)|\sin(x)\sin(y)\geqslant .2 \text{ and } 0\leqslant x,y\leqslant\pi\}$ and a vector field (u^*,v^*) to be the sum of a divergent-free vector field and a gradient field:

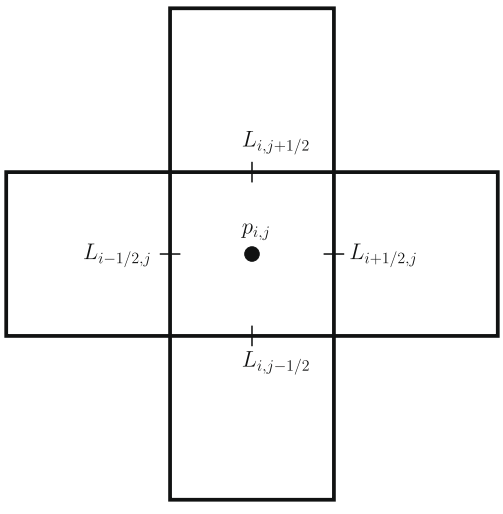

Fig. 2. Cells involved in the construction of the linear system for node (i,j). The densities $\rho_{i\pm\frac{1}{2},j\pm\frac{1}{2}}$ are located at the same location as the length fractions $L_{i\pm\frac{1}{2},j\pm\frac{1}{2}}$.

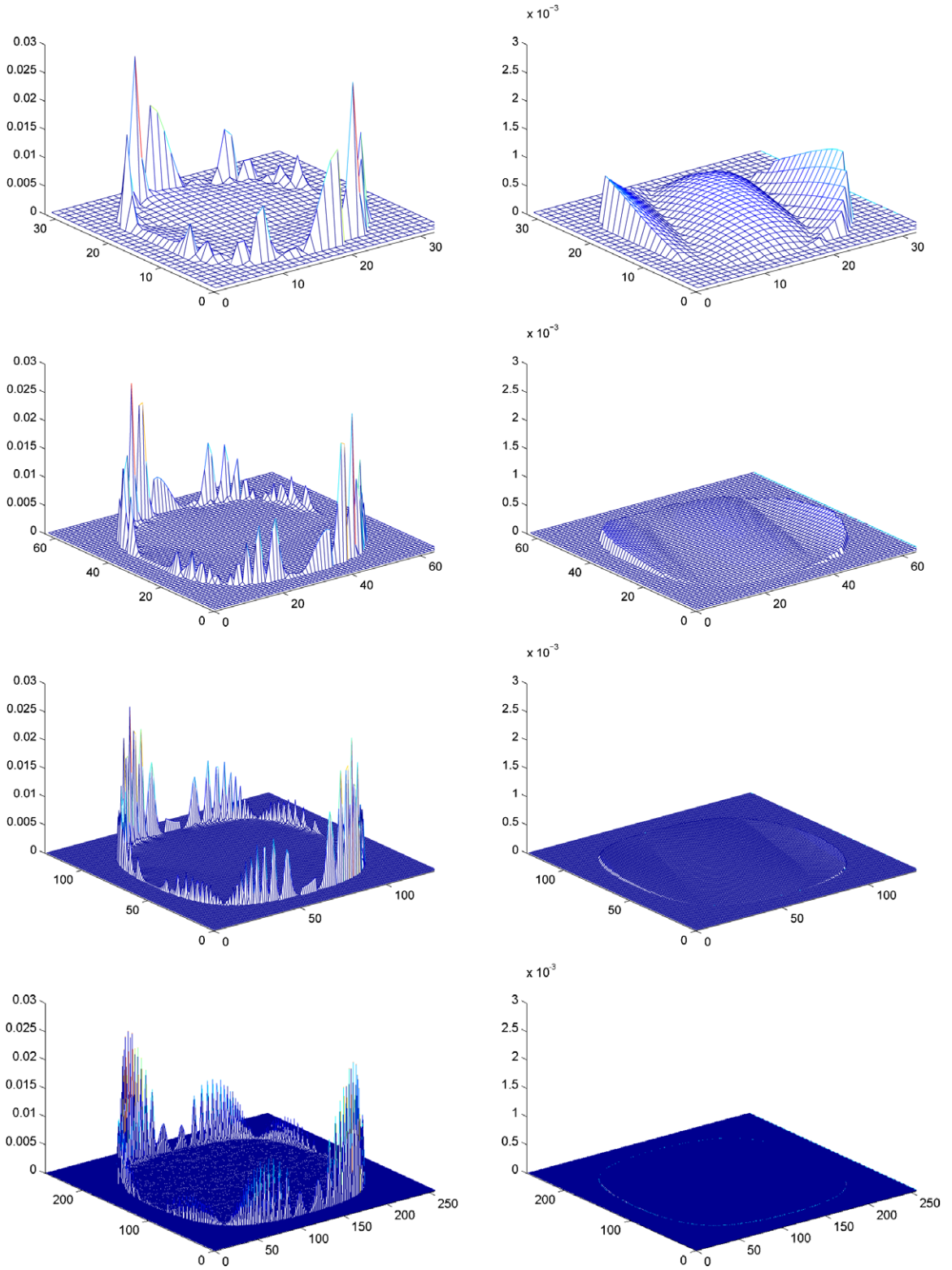

Fig. 3. Error of the Hodge decomposition in the case of [2] (left) and the present work (right) for the grid resolutions 32, 64, 128, and 256. Note that the scales for the figures on the right are an order of 10 smaller than those on the left. In the case of [2], the maximum error is mostly concentrated near the domain's boundary. In addition, the maximum error will not decrease as the grid is refined, as demonstrated in Table 2. In the present work, the maximum error is not necessarily near the domain's boundary. In addition, the maximum error decreases with second-order accuracy as the grid is refined, as shown in Table 1.

$$u^* = \sin(x)\cos(y) + (x^2 - x)(y^3/3 - y^2/2),$$
$$v^* = -\cos(x)\sin(y) + (y^2 - y)(x^3/3 - x^2/2).$$

We apply our projection method on (u^*, v^*) and compare the solution with the exact solution of the divergent-free vector field inside the irregular domain. In this example we take $\mathbf{U}_{bc} \cdot \mathbf{n} = 0$ on Γ. Table 1 demonstrates the second-order accuracy of our Hodge decomposition method in the L^1 and L^∞ norms.

3.3. Stability analysis

The Hodge decomposition states that a smooth vector field $\mathbf{U}^*$ in a domain Ω^- can be decomposed as the sum of a divergence-free vector field $\mathbf{U}$ and a gradient field ∇p, i.e. $\mathbf{U}^* = \mathbf{U} + \nabla p$, with $\nabla \cdot \mathbf{U} = 0$. On the boundary $\partial\Omega$, we assume a Neumann condition for the pressure, $\nabla p \cdot \mathbf{n} = 0$, and the impenetrability condition for the velocity field, $\mathbf{U} \cdot \mathbf{n} = 0$. Therefore, denoting $\langle \cdot, \cdot \rangle_2$ as the L^2-inner product operator on Ω^-, we have

$$\langle \mathbf{U}, \nabla p \rangle_2 = -\langle p, \nabla \cdot \mathbf{U} \rangle_2 + \langle p, \mathbf{U} \cdot \mathbf{n} \rangle_2 = 0,$$

which demonstrates the orthogonality between $\mathbf{U}$ and ∇p. From this, the analytical L^2-stability condition follows since:

$$\|\mathbf{U}^*\|_2^2 = \|\mathbf{U} + \nabla p\|_2^2 = \langle \mathbf{U}, \mathbf{U} \rangle_2 + 2\langle \mathbf{U}, \nabla p \rangle_2 + \langle \nabla p, \nabla p \rangle_2 = \|\mathbf{U}\|_2^2 + \|\nabla p\|_2^2 \Longleftrightarrow \|\mathbf{U}\|_2^2 \leqslant \|\mathbf{U}^*\|_2^2.$$

Likewise, a discrete analog of the L^2-stability condition can be formulated along the same lines. Let $\mathbf{p}$ denote the vector consisting of the scalar p_{ij} sampled at the grid centers, and $\mathbf{U}$ denote the vector combining the horizontal $(u_{i+\frac{1}{2}j})$ and the vertical $(v_{ij+\frac{1}{2}})$ velocity components sampled at the respective grid faces. Let G and D be the standard central difference discretizations of the gradient and divergence operators on the MAC grid, respectively. These discretizations define matrices mapping vectors at grid centers to vectors at grid faces, and vice versa. Let L be the scalar multiplication by $l_{i+\frac{1}{2}j}/\Delta y$ and $l_{ij+\frac{1}{2}}/\Delta x$ at the grid faces. Obviously the operations G, D, and L are linear and the associated matrices satisfy the relations $D = -G^T$ and $L = L^T$.

Now, given a vector field $\mathbf{U}^*$ at grid faces, our projection produces the following linear system:

$$DLG\mathbf{p} = DL\mathbf{U}^*.$$

Once the solution vector $\mathbf{p}$ is obtained from this linear system, $\mathbf{U}$ is calculated as $\mathbf{U} = \mathbf{U}^* - G\mathbf{p}$. The matrix L is diagonal and positive in Ω^-, and one can define the weighted inner product $\langle \mathbf{U}, \mathbf{V} \rangle_L = \langle L\mathbf{U}, \mathbf{V} \rangle_2$ under which we can demonstrate the orthogonality between the vectors $G\mathbf{p}$ and $\mathbf{U}$:

$$\begin{aligned}\langle G\mathbf{p}, \mathbf{U} \rangle_L &= \langle G\mathbf{p}, \mathbf{U}^* - G\mathbf{p} \rangle_L = \langle G\mathbf{p}, \mathbf{U}^* \rangle_L - \langle G\mathbf{p}, G\mathbf{p} \rangle_L = \langle \mathbf{p}, G^T\mathbf{U}^* \rangle_L - \langle G\mathbf{p}, G\mathbf{p} \rangle_L = -\langle \mathbf{p}, D\mathbf{U}^* \rangle_L - \langle G\mathbf{p}, G\mathbf{p} \rangle_L \\ &= -\langle \mathbf{p}, DG\mathbf{p} \rangle_L - \langle G\mathbf{p}, G\mathbf{p} \rangle_L = \langle G\mathbf{p}, G\mathbf{p} \rangle_L - \langle G\mathbf{p}, G\mathbf{p} \rangle_L = 0.\end{aligned}$$

From the orthogonality condition, we have $\|\mathbf{U}^*\|_L^2 = \|\mathbf{U}\|_L^2 + \|\nabla \mathbf{p}\|_L^2$, where $\|\cdot\|_L$ denotes the vector 2-norm under the weight L. The stability condition follows trivially as in the analytical case, $\|\mathbf{U}\|_L \leqslant \|\mathbf{U}^*\|_L$. Thus, we conclude that the projection method is numerically stable.

Fig. 4 depicts the evolution of the log of the L^∞ and L^1 norms of the error in the projected vector field u after repeated projections and illustrates the stability of the method. Here we use the same test problem as in Section 3.2.

3.4. Accuracy analysis

The linear system $DLG\mathbf{p} = DL\mathbf{U}^*$ approximates the Poisson equation $\nabla \cdot \nabla p = \nabla \cdot U^*$. The operation G approximates the gradient with the second-order accuracy, since it is implemented as the central finite differences. The operation DL approximates the divergence operator. Away from the interface, the fraction L is uniformly equal to one, thus DL is nothing but the standard divergence operation D that is second-order accurate. On a grid cell intersecting the boundary $\partial\Omega$, DL is discretized using an integral. On a face $I_{i-\frac{1}{2}j} = x_{i-\frac{1}{2}} \times (y_{j-\frac{1}{2}}, y_{j+\frac{1}{2}})$, the integral is approximated by the quadrature rule

Table 1
Convergence of the horizontal velocity in the case of the present Hodge decomposition on irregular domain.

Grid	L^∞ norm	Order	L^1 norm	Order
16^2	4.29E−3		1.06E−3	
32^2	1.37E−3	1.65	2.67E−4	1.98
64^2	3.22E−4	2.09	6.42E−5	2.06
128^2	7.87E−5	2.03	1.58E−5	2.02
256^2	1.95E−5	2.01	3.92E−6	2.01

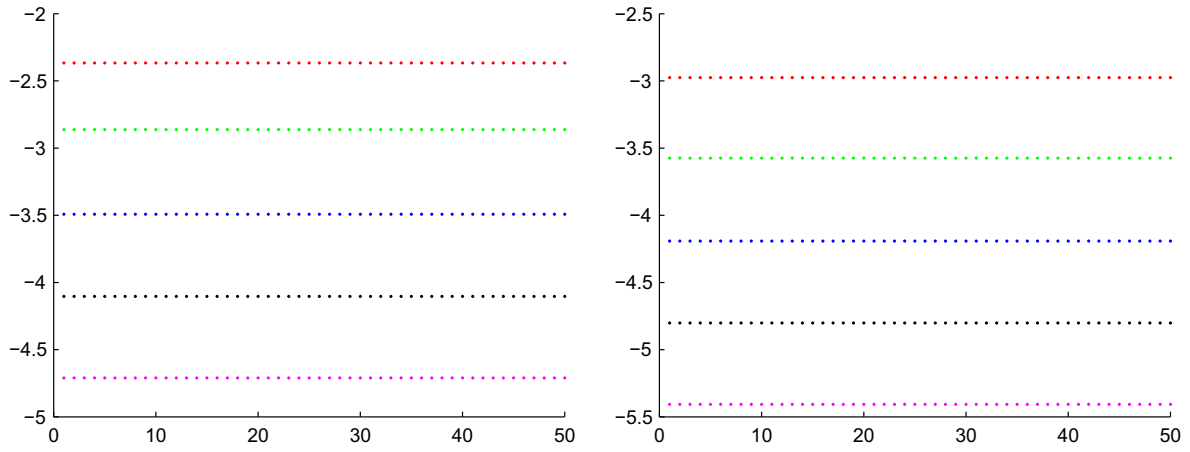

Fig. 4. Evolution of L^∞ (left) and L^1 (right) norms after applying repeatedly the projection described in Section 3, illustrating the stability of our method. The x-axis represents the number of applied projection and the y-axis represents the log of the u-velocity.

$$\int_{I_{i-\frac{1}{2}j}} p_x \simeq l_{i-\frac{1}{2}j} \cdot \frac{p_{ij} - p_{i-1\,j}}{\Delta x}.$$

The quadrature rule is simple and plays an important role in obtaining the symmetric positive definite system, but it is only first-order accurate since in general, the sampling point $(x_{i-\frac{1}{2}}, y_j)$ of the integrand is not located at the middle point of the domain $I_{i-\frac{1}{2}j}$. Therefore, the approximation $DLG\mathbf{p} = DL\mathbf{U}^*$ is first-order accurate at grid cells intersecting the boundary and second-order accurate away from the boundary.

Let $\mathbf{U}^*$ denote the sampling at the grid faces of the analytical vector field U^*, and $\mathbf{p}$ denote the sampling of the analytical solution p_{exct} at grid centers. Since we use a Neumann boundary condition for the pressure, here we impose uniqueness of the solution by taking the solution with zero average. Let $\mathbf{c}$ be the consistency error of the approximation, i.e. $DLG\mathbf{p}_{exct} = DL\mathbf{U}^* + \mathbf{c}$, and $\mathbf{e}$ be the convergence error, i.e. $\mathbf{p}_{exct} = \mathbf{p} + \mathbf{e}$. Subtracting $DLG\mathbf{p} = DL\mathbf{U}^*$ from $DLG\mathbf{p}_{exct} = DL\mathbf{U}^* + \mathbf{c}$ results in

$$DLG\mathbf{e} = \mathbf{c},$$
$$\mathbf{e} = -(-DLG)^{-1}\mathbf{c}.$$

As shown in Section 3.1, the matrix $-DLG$ is symmetric positive definite, having positive diagonal elements and non-positive off-diagonal elements, and is thus an M-matrix. The convergence error is thus minus the multiplication of the inverse of the M-matrix with the consistency error. The consistency error is second-order accurate away from the boundary, and is first-order accurate near the boundary. Although the consistency error is first-order accurate near the boundary, the convergence error is uniformly second-order accurate, and this is referred as supra-convergence. This configuration has occurred in many elliptic problems such as in Shortley–Weller [24], Johansen and Colella [12], and Min and Gibou [19], in all of which the convergence error is second-order accurate in the maximum norm. The supra-convergence seems to be based on the property of an M-matrix: the inverse of an M-matrix is a non-negative matrix, and its multiplication behaves like an averaging process. The boundary is geometrically one dimension less than the domain so that the number of grid cells near the interface is one-order less than the number of grid cells away from the interface.

Let h be the grid spacing. The consistency error $\mathbf{c}$ is $O(h)$ near the boundary, and $O(h^2)$ away from the interface, and the number of grid cells near the interface is $O(h^{-1})$ whereas the number of grid cells away from the interface is $O(h^{-2})$. The matrix $(-DLG)^{-1}$ is non-negative, and is a numerical analog of Δ^{-1}. Since Δ^{-1} is an integral operator, we assume that each element of the matrix $(-DLG)^{-1}$ is $O(h^2)$. Now, for each grid point (i,j) we have

$$\mathbf{e}_{ij} = \sum_k (-DLG)^{-1}_{ik}\mathbf{c}_{kj} = \sum_{\substack{\text{node } k: \\ \text{away from boundary}}} (-DLG)^{-1}_{ik}\mathbf{c}_{kj} + \sum_{\substack{\text{node } k: \\ \text{near boundary}}} (-DLG)^{-1}_{ik}\mathbf{c}_{kj}$$
$$= O(h^{-2}) \cdot O(h^2) \cdot O(h^2) + O(h^{-1}) \cdot O(h^2) \cdot O(h^1) = O(h^2).$$

Thus we showed that the convergence error is second-order accurate in the maximum norm, but we emphasize that our derivation is rigorous under the assumption that the matrix elements $(-DLG)^{-1}$ are $O(h^2)$. This assumption was verified using an eigenvalue analysis in the case of the Shortley–Weller's method. In the case of our discretization, the matrix is more complex and the eigenvalue analysis is currently beyond the scope of this paper.

We have therefore demonstrated that the scalar variable $\mathbf{p}$ is second-order accurate. Since the differentiation divides the scalar by a grid size, its gradient $G\mathbf{p}$ should be first-order accurate, and the projection $\mathbf{U} = \mathbf{U}^* - G\mathbf{p}$ should also be first-order

accurate. This is exactly observed in our three spatial dimensions examples. However we observed instead second-order accurate solutions in two spatial dimensions with the non-penetration condition $\mathbf{U}\cdot\mathbf{n}=0$. This boost in accuracy in two spatial dimensions only was also reported and analyzed in the case of the Shortley–Weller's method, but in our case, the matrix is more complex and the analysis is also currently beyond the scope of this paper.

4. A link with the minimization approach of Batty et al.

The work of Batty et al. [2] is based on minimizing the total kinetic energy of the system, i.e.

$$KE=\int_{\Omega}\frac{1}{2}\rho|u^2|+\frac{1}{2}\mathbf{V}^*\mathbf{M}_s\mathbf{V},$$

where $\mathbf{V}$ is the velocity vector of a solid object and $\mathbf{M}_s$ is the mass linear operator matrix containing the inertia tensor and mass of the solid. In one spatial dimension, Batty et al. [2] showed that this approach leads to the following linear system:

$$\frac{m_{i+\frac{1}{2}}\frac{p_{i,j}-p_{i+1,j}}{\Delta x}+m_{i-\frac{1}{2}}\frac{p_{i,j}-p_{i-1,j}}{\Delta x}}{\Delta x}=\frac{m_{i+\frac{1}{2}}u_{i+1/2}+m_{i-\frac{1}{2}}u_{i-1/2}}{\Delta x},$$

where $m_{i+\frac{1}{2}}$ refers to the mass fraction of fluid in the cell $C_{i,j}$ and can be computed as $m_{i+\frac{1}{2}}=\int_{C_{ij}\cap\Omega}\rho\,dV$. A few choices on how to compute this integral are given in [2]. This approach can therefore be interpreted as the standard central differencing approximation of

$$-\nabla\cdot(m\nabla p)=-\nabla\cdot(mu^*),$$

where the negative sign has been introduced to make the system positive definite. In contrast, our approach is an approximation of

$$-\nabla\cdot(L\nabla p)=-\nabla\cdot(Lu^*),$$

where L is the *length fractions* of the cell's faces occupied by the fluid instead of the *mass* as in the case of Batty et al. [2] (see Fig. 1).

Considering the same example as in Section 3.2, we find that the scheme in [2] is only first-order accurate in the average L^1 norm and is not convergent in the L^∞ norm, as illustrated in Table 2. In order to compute the masses $m_{i+\frac{1}{2}}$, we used the robust second-order accurate method of Min and Gibou [17] to compute the integrals. Fig. 3 also demonstrates that the error is maximum near the solid object. Since this error does not converge, this method is ill-advised for computations where the velocity field near objects is important.

5. Solving Navier–Stokes equations on irregular domains

In what follows, we describe how to use the novel discretization of Section 3 for the numerical approximation of the Navier–Stokes equations on irregular domains. We choose a semi-Lagrangian scheme for approximating the momentum and a Backward Difference Formula scheme for evolving the equations in time, as described in [16]:

$$\frac{3}{2}\mathbf{U}^*-2\mathbf{U}_d^n+\frac{1}{2}\mathbf{U}_d^{n-1}=\Delta t\mu\nabla^2\mathbf{U}^*+\Delta tF^{n+1}\quad\text{in }\Omega^-,\tag{3}$$

$$\mathbf{U}_{bc}^*=\mathbf{U}_{bc}^{n+1}+\Delta t\nabla p^n\quad\text{on }\Gamma,\tag{4}$$

where the variables have been rescaled by ρ. The intermediate velocity field $\mathbf{U}^*$ is then projected onto the divergence free field:

$$\mathbf{U}^{n+1}=\mathbf{U}^*+\Delta t\nabla p^{n+1},$$

where the scalar function p^{n+1} is found with the discretization presented in Section 3. The semi-Lagrangian Backward Difference Formula (SL-BDF) method guarantees unconditional stability, but we emphasize that the projection method of

Table 2
Convergence of the horizontal velocity in the case of the minimization approach of [2].

Grid	L^∞ norm	Order	L^1 norm	Order
16^2	3.87E−2		3.20E−3	
32^2	3.40E−2	0.13	1.45E−3	0.79
64^2	3.96E−2	−0.15	5.75E−4	0.92
128^2	4.91E−2	−0.22	2.70E−4	0.76
256^2	8.16E−2	−0.51	1.78E−4	0.42

Section 3 can be straightforwardly combined with other methods for discretizing the momentum or evolving the equations in time. In the next few sections, we describe the required steps in details.

5.1. SL-BDF method

Since we are considering incompressible flows, for which shock and rarefaction waves do not occur, we can use an implicit scheme based on the method of characteristics to update the velocity field in time. The method of characteristics state that $\mathbf{U}^{n+1}(x^{n+1}) = \mathbf{U}^n(x_d)$, where x^{n+1} is any grid node and x_d is the corresponding departure point from which the characteristic curve originates. We use the second order mid-point method for locating the departure point, as in Xiu and Karniadakis [25]:

$$\hat{x} = x^{n+1} - \frac{\Delta t}{2} \cdot \mathbf{U}^n(x^{n+1}),$$
$$x_d = x^{n+1} - \Delta t \cdot \mathbf{U}^{n+\frac{1}{2}}(\hat{x}),$$

where we define the velocity at the mid-time step $t^{n+\frac{1}{2}}$ by a linear combination of the velocities at the two previous time steps, i.e. $\mathbf{U}^{n+\frac{1}{2}} = \frac{3}{2}\mathbf{U}^n - \frac{1}{2}\mathbf{U}^{n-1}$. Since $\hat{x}$ and x_d are not on grid nodes in general, $\mathbf{U}^{n+\frac{1}{2}}(\hat{x})$ and $\phi^n(x_d)$ are found by interpolation. As noted in Min and Gibou [18], it is enough to define $\mathbf{U}^{n+\frac{1}{2}}(\hat{x})$ with a multilinear interpolation, e.g.:

$$u(x,y) = u(0,0)(1-x)(1-y) + u(0,1)(1-x)(y) + u(1,0)(x)(1-y) + u(1,1)(x)(y),$$

where the interpolation is written for a scaled cell $C = [0,1]^2$. On the other hand, $\mathbf{U}^n(x_d)$ is approximated with the non-oscillatory quadratic interpolation described in the next section.

5.2. Stabilized quadratic interpolation

Lagrange-type interpolation procedures are sensitive to nearby discontinuities in the solution or its derivatives, as noted in [18]. In order to produce stable results, we therefore favor quadratic interpolations with a correction term using an approximation to the second-order derivatives. For a cell $[0,1]^2$ and a function u, we have:

$$u(x,y) = u(0,0)(1-x)(1-y) + u(0,1)(1-x)(y) + u(1,0)(x)(1-y) + u(1,1)(x)(y) - u_{xx}\frac{x(1-x)}{2} - u_{yy}\frac{y(1-y)}{2},$$

where we define

$$u_{xx} = \min_{v \in \text{nodes}(C)} (|D^0_{xx} u_v|),$$
$$u_{yy} = \min_{v \in \text{nodes}(C)} (|D^0_{yy} u_v|),$$
$$D^0_{xx} u_v = \frac{u_{i+1,j} + u_{i-1,j} - 2u_{i,j}}{\Delta x^2} \quad \text{for node } v \text{ at index } (i,j),$$
$$D^0_{yy} u_v = \frac{u_{i,j+1} + u_{i,j-1} - 2u_{i,j}}{\Delta y^2} \quad \text{for node } v \text{ at index } (i,j).$$

Choosing the minimum between the second-order derivatives enhances the numerical stability of the interpolation, especially in region where u presents kinks.

5.3. Implicit viscosity

We treat the viscous term of Eq. (3) implicitly. The discretization of the viscous term is similar to that of a Poisson equation given by

$$\beta \nabla^2 \mathbf{U}^* = \mathbf{f} \quad \text{in } \Omega^-,$$

where $\beta = \Delta t \mu$ is a positive constant. We impose a Dirichlet boundary condition of $\mathbf{U}_{bc} = 0$ at the solid boundary Γ, and $\mathbf{U}^*_{bc}$ is calculated from Eq. (4). We use the approach introduced by Gibou et al. [9] to obtain a symmetric implicit discretization. For the sake of clarity, we summarize the approach here and refer the interested reader to [9] for more details.

5.3.1. Discretization of the poisson equation on irregular domains

In this section, we recall the discretization of the Poisson equation on irregular domains, as described in Gibou et al. [9]. The discretization of the Poisson equation, including the special treatments needed at the interface, is performed in a dimension by dimension fashion. Therefore, without loss of generality, we only describe the discretization in one spatial dimension for the βu_{xx} term. In multiple spatial dimensions, the βu_{yy} and βu_{zz} terms are each independently discretized in the same manner as βu_{xx}.

Consider the Poisson equation in one spatial dimension

$$u_{xx} = f, \tag{5}$$

where the variables have been rescaled by the constant β, with a Dirichlet boundary condition of $u = u_I$ on the interface where $\phi = 0$. The computational domain is discretized into cells of size Δx with the grid nodes x_i located at the cell centers. The cell edges are referred to as fluxes so that the two fluxes bounding the grid node x_i are located at $x_{i\pm\frac{1}{2}}$. The solution of the Poisson equation is computed at the grid nodes and is written as $u_i = u(x_i)$. We consider the standard second-order discretization for Eq. (5), given by

$$\frac{\left(\frac{u_{i+1}-u_i}{\Delta x}\right) - \left(\frac{u_i-u_{i-1}}{\Delta x}\right)}{\Delta x} = f_i, \tag{6}$$

where u_x is discretized at the flux locations.

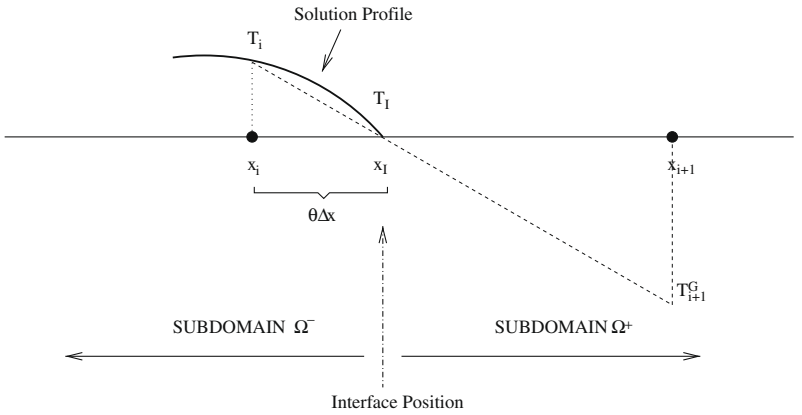

Fig. 5. Definition of the ghost cells with linear extrapolation. First, we construct a linear interpolant $\tilde{u}(x) = ax + b$ of u such that $\tilde{u}(0) = u_i$ and $\tilde{u}(\theta\Delta x) = u_I$. Then we define $u^G_{i+1} = \tilde{u}(\Delta x)$.

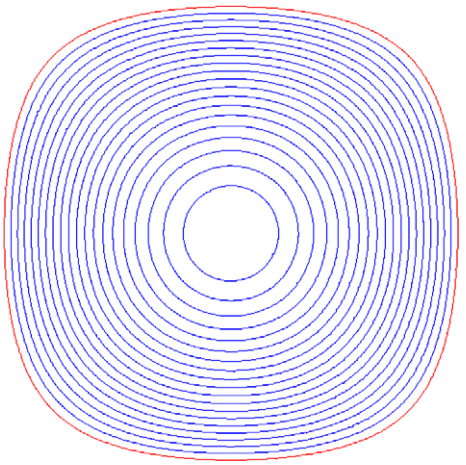

Fig. 6. Streamlines of the flow, for example, Section 6.1

Table 3
Convergence of the horizontal velocity in the case of the Navier–Stokes example on irregular domain, for example, Section 6.1.

Grid	L^∞ norm	Order	L^1 norm	Order
16^2	2.44E−3		6.74E−4	
32^2	1.00E−3	1.29	2.22E−4	1.60
64^2	4.51E−4	1.15	7.33E−5	1.60
128^2	1.29E−4	1.81	1.91E−5	1.94
256^2	3.31E−5	1.95	4.95E−6	1.95

In order to avoid differentiating the fluxes across the interface where the solution presents a kink, a ghost value is used: referring to Fig. 5, let x_I be an interface point between grid points x_i and x_{i+1} with a Dirichlet boundary condition of $u = u_I$ applied at x_I. We define a ghost value u^G_{i+1} at x_{i+1} across the interface, and rewrite Eq. (6) as

$$\frac{\left(\frac{u^G_{i+1}-u_i}{\Delta x}\right) - \left(\frac{u_i-u_{i-1}}{\Delta x}\right)}{\Delta x} = f_i. \tag{7}$$

The ghost value u^G_{i+1} is defined by first constructing an interpolant $\tilde{u}(x)$ of $u(x)$ on the left of the interface, such that $\tilde{u}(0) = u_i$, and then defining $u^G_{i+1} = \tilde{u}(\Delta x)$. Fig. 5 illustrates the definition of the ghost cells in the case of the linear extrapolation. In this work, we employ the linear extrapolation in order to obtain a symmetric discretization that remains second-order accurate, as elaborated on in [9]. The linear extrapolation is defined by $\tilde{u}(x) = ax + b$ with $\tilde{u}(0) = u_i$ and $\tilde{u}(\theta\Delta x) = u_I$, where $\theta \in [0, 1]$ refers to the cell fraction occupied by the subdomain Ω^-. Substituting for u^G_{i+1} in Eq. (8) gives a symmetric discretization of

$$\frac{\left(\frac{u_I-u_i}{\theta\Delta x}\right) - \left(\frac{u_i-u_{i-1}}{\Delta x}\right)}{\Delta x} = f_i. \tag{8}$$

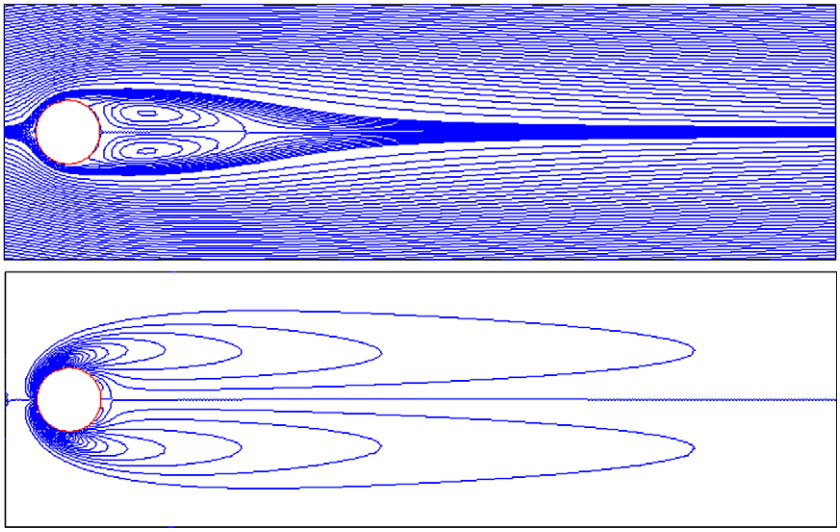

Fig. 7. Stationary state: contours of the stream function and of the vorticity for $Re = 40$, for example, Section 6.2. The box in the figure is $[7,20] \times [6,10]$. Contour levels for the stream function are $[-5 : 0.05 : 5]$ and $[-0.05 : 0.005 : 0.05]$. Contour levels for the vorticity are $[-1 : 0.4 : 1]$.

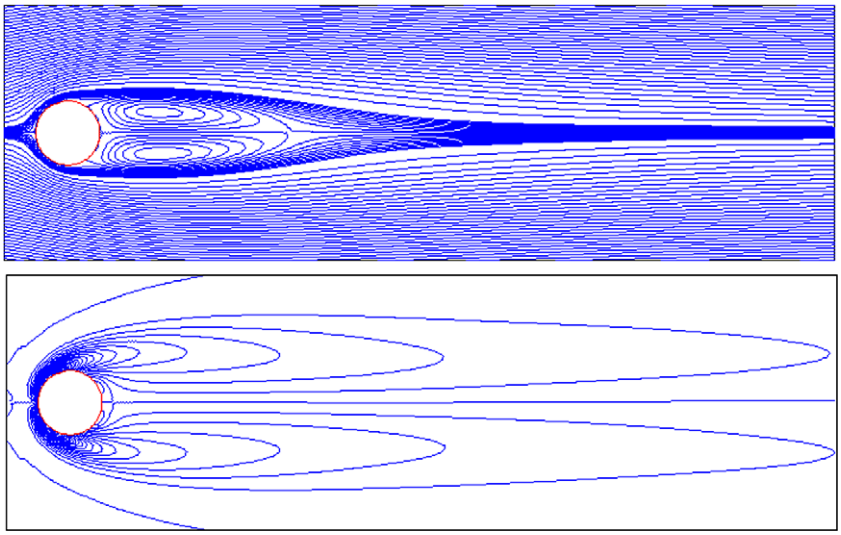

Fig. 8. Transition state: contours of the stream function and of the vorticity for $Re = 50$, for example, Section 6.2 at $t = 100$. Contour levels and the dimensions of the box are the same as those in Fig. 7. The flow does not become stationary, and shows vertical asymmetry.

5.3.2. Location of the interface

Referring to Fig. 5, we compute the location of the interface between x_i and x_{i+1} by finding the zero crossing of the quadratic interpolant $\phi = \phi(x_i) + \phi_x(x_i)x + \frac{1}{2}\phi_{xx}(x_i)x^2$. We note that the quadratic interpolant in ϕ is convex with a positive second-order derivative. The location of the interface along the x-direction is calculated as:

$$\theta\Delta x = \begin{cases} \frac{-\phi_x(x_i)+\sqrt{\phi_x^2(x_i)-2\phi_{xx}(x_i)\phi(x_i)}}{\phi_{xx}(x_i)} & \text{if } \phi_{xx}(x_i) > \epsilon, \\ -\frac{\phi(x_i)}{\phi_x(x_i)} & \text{if } |\phi_{xx}(x_i)| \leqslant \epsilon, \end{cases} \tag{9}$$

where ϵ is a small positive number to avoid division by zero. $\phi_x(x_i)$ and $\phi_{xx}(x_i)$ are approximated at x_i using second-order accurate central difference schemes.

5.4. Extrapolation procedures on irregular domains

The procedure to update the intermediate velocity requires interpolation procedures that may need valid values for $\mathbf{U}^n$ outside Ω^-. Likewise, the procedure to update the intermediate velocity only defines $\mathbf{U}^*$ in the irregular domain Ω^- but needs to be extrapolated in a band outside Ω^- in order to apply the projection step described in Section 3. In [1], Aslam introduced a high-order accurate extrapolation method on irregular domain to the whole domain, and [18] improved the efficiency of the method by lowering the unnecessarily high order of finite differences to enhance numerical stability. In what follows, we present a method heavily based on Aslam [1] and the variants of [18], to include the boundary condition $\mathbf{U}_{bc}$ at the interface.

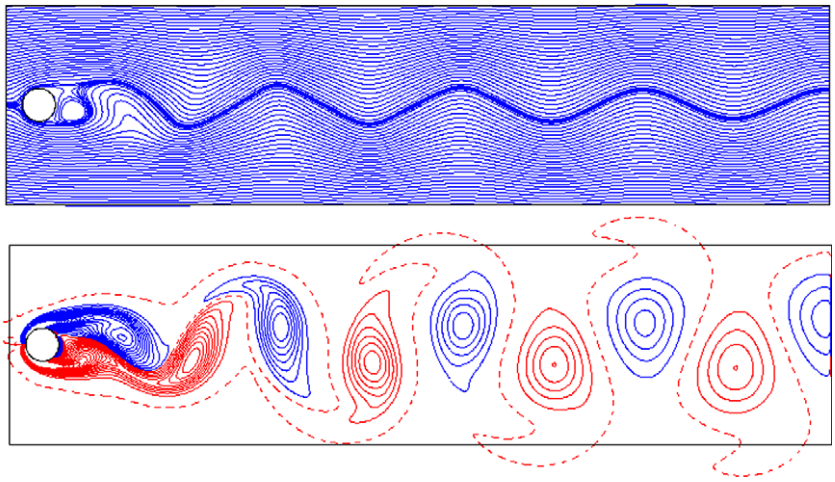

Fig. 9. Unsteady vortex shedding state: contours of the stream function and of the vorticity for $Re = 100$, for example, Section 6.2 at $t = 100$. The box in the figure is $[7,32] \times [5,11]$. Contour levels for the stream function are $[-5 : 0.1 : 5]$ and $[-0.05 : 0.015 : 0.05]$. Contour levels for the vorticity are $[-4 : 0.2 : 4]$.

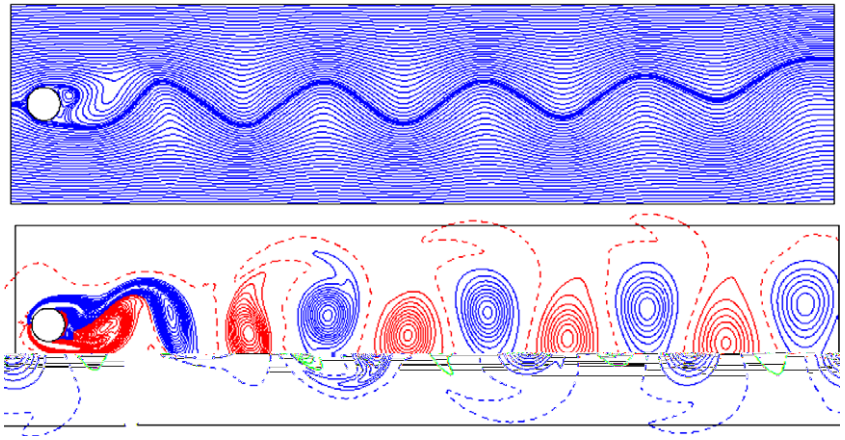

Fig. 10. Unsteady vortex shedding state: contours of the stream function and of the vorticity for $Re = 200$, for example, Section 6.2 at $t = 100$. Contour levels and the dimensions of the box are the same as those in Fig. 9.

Consider a quantity $Q(x)$ given inside an irregular domain $\Omega^- = \{x|\phi(x) \leqslant 0\}$, where ϕ is a higher dimensional level set function [20,23]. In order to extend this quantity to third order accuracy, Aslam proposed the following steps in [1]. First, the normal vector field $n = \frac{\nabla\phi}{|\nabla\phi|}$ is calculated in the whole domain with the standard central finite difference formulas. Then directional derivatives $Q_n = n \cdot \nabla Q$ and $Q_{nn} = n \cdot \nabla Q_n$ are successively calculated with standard central finite difference

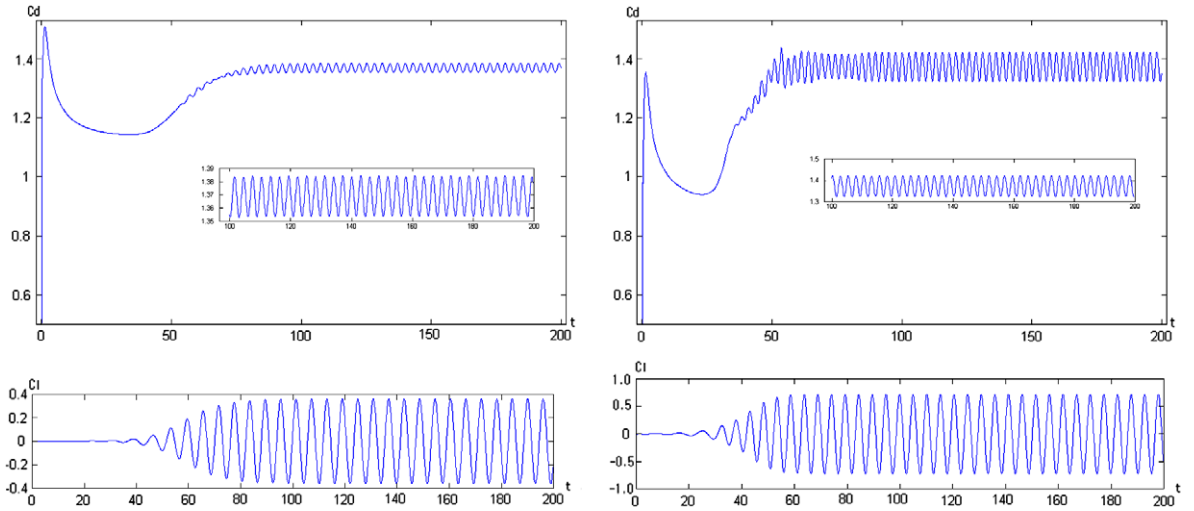

Fig. 11. Time-dependent drag and lift coefficients, for example, Section 6.2. (Top Left) Drag, $Re = 100$; (Top right) Drag, $Re = 200$; (Bottom left) Lift, $Re = 100$; (Bottom right) Lift, $Re = 200$.

Table 4
Drag and lift coefficients, for example, Section 6.2.

	Drag(C_D)		Lift(C_L)	
	$Re = 100$	$Re = 200$	$Re = 100$	$Re = 200$
Belov et al. [3]	–	1.19 ± 0.042	–	±0.64
Braza et al. [4]	1.364 ± 0.015	1.40 ± 0.05	±0.25	±0.75
Liu et al. [15]	1.350 ± 0.012	1.31 ± 0.049	±0.339	±0.69
Calhoun [5]	1.330 ± 0.014	1.172 ± 0.058	±0.298	±0.668
Present	1.368 ± 0.016	1.373 ± 0.050	±0.360	±0.724

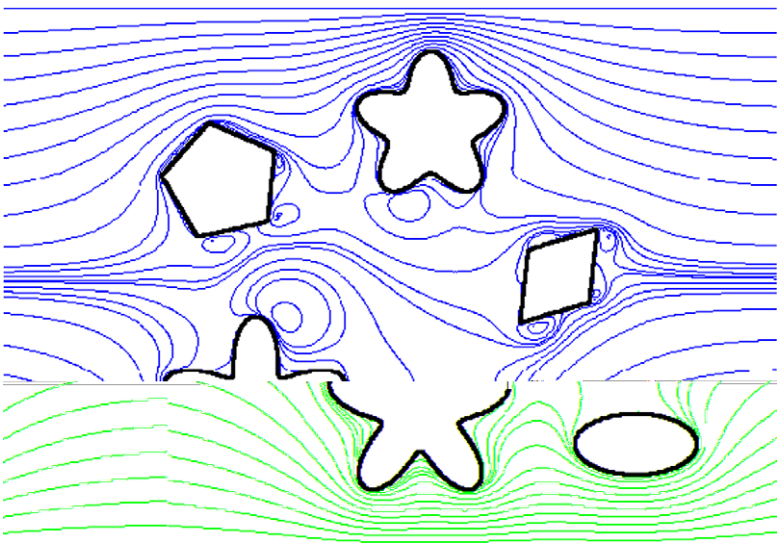

Fig. 12. Streamlines, for example, Section 6.3 at steady state with $\mu = 0.01$.

formulas. Since Q is not defined in the whole domain, Q_n and Q_{nn} at a grid node are properly defined only when Q and Q_n are defined at all of its neighboring nodes. To help in these definitions, numerical Heaviside functions are defined as:

$$H^0_{ij} = \begin{cases} 0 & \text{if } \phi_{ij} \leqslant 0, \\ 1 & \text{otherwise}, \end{cases}$$

$$H^1_{ij} = \begin{cases} 0 & \text{if } H^0_{i\pm1,j} = 0 \text{ and } H^0_{i,j\pm1} = 0, \\ 1 & \text{otherwise}, \end{cases}$$

and

$$H^2_{ij} = \begin{cases} 0 & \text{if } H^1_{i\pm1,j} = 0 \text{ and } H^1_{i,j\pm1} = 0, \\ 1 & \text{otherwise}. \end{cases}$$

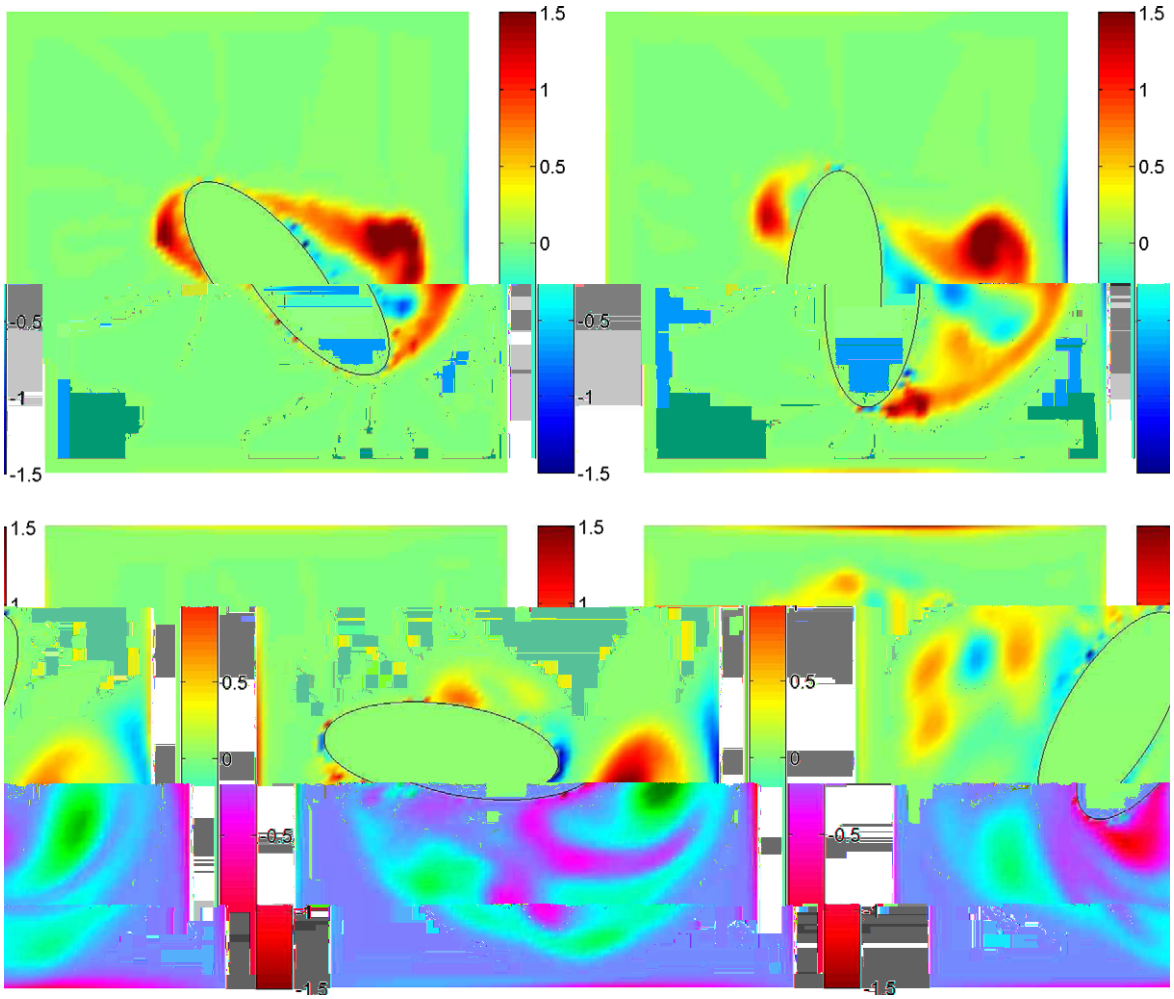

Fig. 13. Vorticity density of fluid flow around the rotating ellipse, for example, Section 6.4 at t=1.5, 3.5, 6.5, and 10.5, going from left to right, top to bottom.

Table 5
Convergence of the velocity in the x- and y-directions in the case of the Navier–Stokes example in three spatial dimensions on irregular domain, for example, Section 7.1.

Grid	L^∞ norm	Order	L^1 norm	Order
8^3	1.51E−2		4.92E−3	
16^3	5.03E−3	1.58	6.20E−4	2.99
32^3	2.49E−3	1.02	2.60E−4	1.25
64^3	7.23E−4	1.78	8.32E−5	1.65
128^3	3.77E−4	0.94	2.41E−5	1.77

Note that Q, Q_n and Q_{nn} are properly defined only when $H^0 = 0, H^1 = 0$, and $H^2 = 0$, respectively. For the second step, the value of Q_{nn} is extended to the whole domain along the normal vector field, via:

$$\frac{\partial Q_{nn}}{\partial \tau} + H_2 \cdot (n \cdot \nabla Q_{nn}) = 0. \tag{10}$$

Third, using the extrapolated value of Q_{nn} in the above step, Q_n is linearly extrapolated to the whole domain along the normal vector field using:

$$\frac{\partial Q_n}{\partial \tau} + H_1 \cdot (n \cdot \nabla Q_n - Q_{nn}) = 0. \tag{11}$$

Table 6
Convergence of the velocity in the z-direction in the case of the Navier–Stokes example in three spatial dimensions on irregular domain, for example, Section 7.1.

Grid	L^∞ norm	Order	L^1 norm	Order
8^3	2.41E−2		7.55E−3	
16^3	6.02E−3	2.00	7.52E−4	3.33
32^3	2.10E−3	1.52	3.82E−4	0.98
64^3	1.01E−3	1.06	1.23E−4	1.64
128^3	4.90E−4	1.04	3.58E−5	1.78

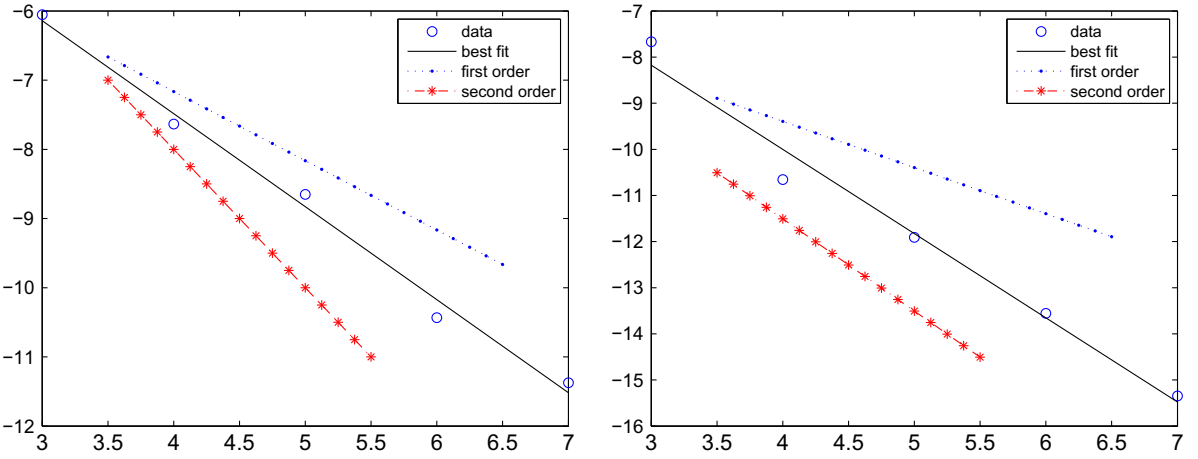

Fig. 14. Log–log plots of the L^∞ (left) and L^1 (right) norms of the x and y components of velocity as a function of grid resolution, for example, Section 7.1.

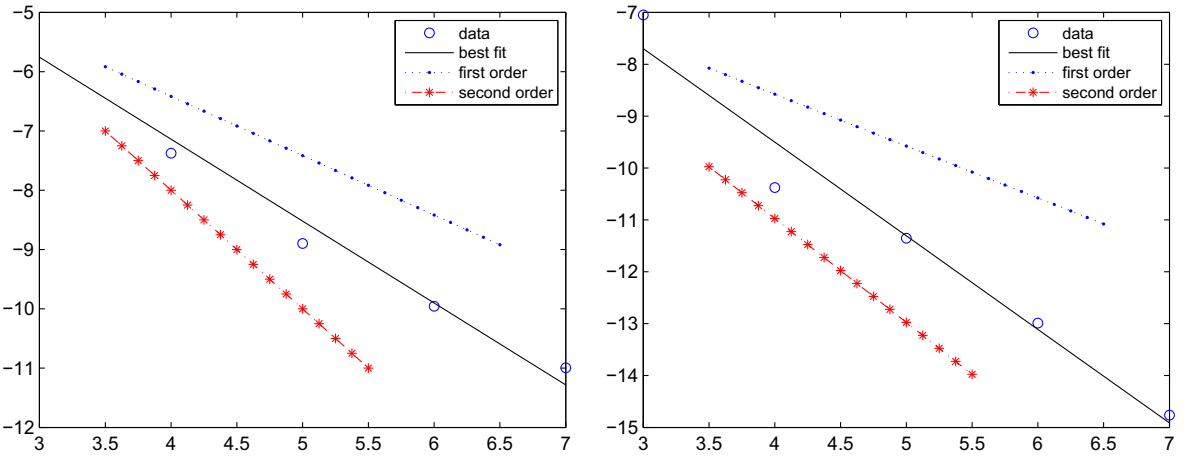

Fig. 15. Log–log plots of the L^∞ (left) and L^1 (right) norms of the z component of velocity as a function of grid resolution, for example, Section 7.1.

Finally, using the extrapolated value of Q_n in the above step, Q is quadratically extrapolated to the whole domain along the normal vector field:

$$\frac{\partial Q}{\partial \tau} + H_0 \cdot (n \cdot \nabla Q - Q_n) = 0. \tag{12}$$

In [18], Min and Gibou introduced efficient discretizations for the above equations, and found that in order to obtain third order accuracy for the extrapolated quantity Q near the interface, it is enough to apply a TVD RK-2 discretization for the time derivative, a first order upwind discretization for the space derivatives in Eqs. (10) and (11), and a second order ENO discretization for the space derivatives in (12).

6. Examples for the Navier–Stokes equations

6.1. Convergence analysis for an exact solution

Consider the Navier–Stokes equations on an irregular domain $\Omega^- = \{(x,y) | \sin(x)\sin(y) \geqslant .2 \text{ and } 0 \leqslant x, y \leqslant \pi\}$ with initial velocity field $\mathbf{U}(x,y,0) = (\sin x \cos y, -\cos x \sin y)$. The boundary condition of the velocity field on the wall is $\mathbf{U}_{bc} \cdot \mathbf{n} = 0$. Fig. 6 depicts the irregular domain and the streamlines of the flow. We take the appropriate forcing term for the exact solution to be $\mathbf{U}(x,y,t) = (\cos t \sin x \cos y, -\cos t \cos x \sin y)$. We take a final time of $\pi/3$. Table 3 shows the second-order accuracy in the L^1 and L^∞ norms.

6.2. Flow past a cylinder

We now consider the simulation of a fluid flow past a cylinder, as first proposed by Dennis and Chang [8], and we show that our method is capable of reproducing the steady and unsteady regimes of the flows. The case where the Reynolds number is relatively small ($Re \approx 40$) corresponds to a steady regime whereas larger Reynolds numbers ($Re \approx 200$) correspond to

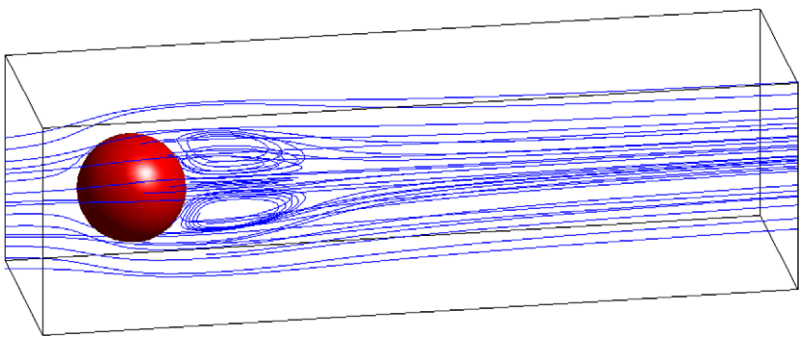

Fig. 16. Steady axisymmetric regime: particle path trace in three spatial dimensions for the $Re = 150$ case, for example, Section 7.2.

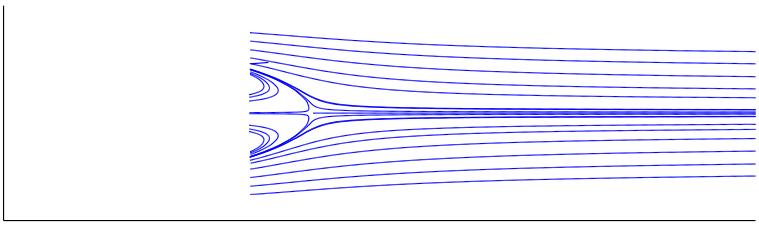

unsteady regimes where vortex shedding can be observed. The transition between those two regimes occurs somewhere between $Re = 40$ and $Re = 50$, as demonstrated experimentally by Coutanceau and Bouard [7].

Consider a domain $\Omega = [0, 32] \times [0, 16]$ and a cylinder with radius $r = .5$ and center located at (8,8). We impose Dirichlet boundary conditions of $u = U_\infty = 1$ on the left, top and bottom walls, an outflux boundary condition at the right wall and the no-slip boundary condition at the cylinder's boundary. In our numerical experiments we define the viscosity coefficient $\mu = 2rU_\infty/Re$ and vary the Reynolds number Re. Fig. 7 depicts the streamlines and vorticity contours for $Re = 40$. In particular, the symmetry of the results are in agreement with a steady regime for low Reynolds numbers. Fig. 8 depicts the streamlines and vorticity contours for $Re = 50$. This experiment illustrates a vertical asymmetry, indicating that the transition to an unstable regime occurs between $Re = 40$ and $Re = 50$. Figs. 9 and 10 illustrate an unstable regime for $Re = 100$ and $Re = 200$,

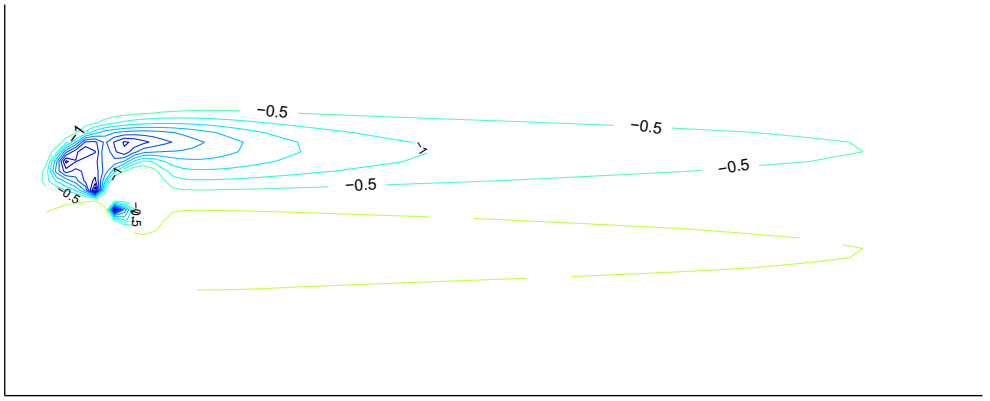

respectively. In particular, they exhibit the broken symmetry of the vorticity contours and the standard vortex shedding. The total force acting on the cylinder is the integration of the force, and given as

$$F = \int_{\Gamma} (-p + 2\mu D)\mathbf{n},$$

where D is the symmetric stress tensor and $\mathbf{n}$ is the outward normal to the cylinder. The drag and the lift coefficients are given by the x- and y-components of the F, respectively, properly scaled by rU_{∞}. Fig. 11 depicts the sinusoidal oscillations of the drag and lift coefficients on the cylinder. The coefficients are in agreement with previously reported results, as shown in Table 4. The integral for computing the force is approximated in this work by the geometric integration of [17].

6.3. Flow past arbitrary shaped solid objects

Consider a domain $\Omega = [-1,1]^2$ with multiple solid obstacles, as done in Ito et al. [11]. We set a no-slip boundary condition on the solids' boundaries, an inflow boundary condition of $(u, v) = (1, 0)$ at $x = -1$ and an outflow boundary condition at $x = 1$. The top and bottom walls have a boundary condition of $(u, v) = (1, 0)$. Fig. 12 depicts the streamlines and the vorticity contours at steady state.

6.4. Ellipse rotating in a closed box

Consider a domain $\Omega = [-1,1]^2$ and an ellipsoid with dimensions $radius_x = .5, radius_y = .2$, centered at $(.2, 0)$ at $t_n = 0$, and rotating around the pivot point $(0,0)$. We impose no-slip boundary conditions all the domain walls and the solid boundary. We define viscosity $\mu = .0001$ and angular velocity $\omega = .5$ in the clockwise. Fig. 13 depicts vorticity density of the fluid flow around the moving object.

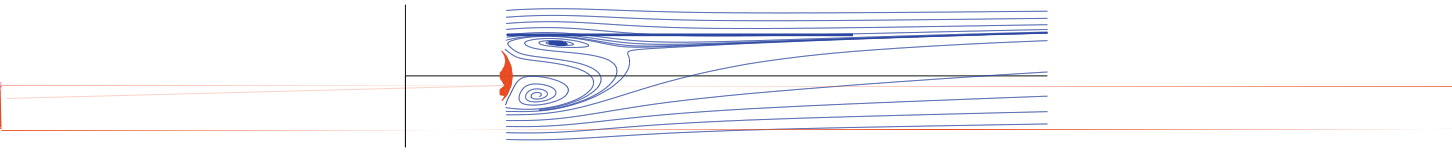

7. Examples for the Navier–Stokes equations in three spatial dimensions

7.1. Convergence analysis for an exact solution

Consider the Navier–Stokes equations on an irregular domain $\Omega^- = \{(x,y,z)| -\cos x \cos y \cos z \geqslant .4 \text{ and } .5\pi \leqslant x,y,z \leqslant 1.5\pi\}$ with initial velocity field $\mathbf{U}(x,y,z,0) = (\cos x \sin y \sin z, \sin x \cos y \sin z, -2\sin x \sin y \cos z)$. The boundary condition of the velocity field on the interface is $\mathbf{U}_{bc} \cdot \mathbf{n} = 0$. We take the appropriate forcing term for the exact solution to be $\mathbf{U}(x,y,z,t) = (\cos t \cos x \sin y \sin z, \cos t \sin x \cos y \sin z, -2\cos t \sin x \sin y \cos z)$. We take a final time of $\pi/3$. Tables 5 and 6 show the first-order accuracy in the L^∞ and L^1 norms. Figs. 14 and 15 show the log–log plot of the L^∞ and L^1 norms against grid resolution.

7.2. Flow past a sphere

We now consider the simulation of a fluid flow past a sphere, as previously done by Johnson and Patel in [13], and show that our method is capable of reproducing the steady axisymmetric flow and steady non-axisymmetric flow regimes. Steady axisymmetric flow occurs at relatively low Reynolds number ($Re \approx 150$) while the steady non-axisymmetric flow occurs at larger Reynolds numbers ($Re \approx 250$). The transition between those two regimes occurs somewhere between $Re = 200$ and $Re = 210$.

Consider a domain $\Omega = [0,16] \times [0,8] \times [0,8]$ and a sphere with radius $r = .5$ and center located at (4,4,4). We impose a Dirichlet boundary condition of $u = U_\infty = 1$ on the left, top, bottom, front, and back walls, an outflux boundary condition at the right wall and the no-slip boundary condition at the sphere's boundary. We define the viscosity coefficient $\mu = 2rU_\infty/Re$ and vary the Reynolds number Re. Fig. 16 depicts the particle path trace for a steady axisymmetric flow in three spatial dimensions at $Re = 150$. Figs. 17 and 18 depict the streamlines and vorticity contours at $Re = 150$. In particular, the symmetry of the results are in agreement with a steady axisymmetric flow regime for lower Reynolds numbers, and are comparable to the results from Johnson and Patel [13]. Fig. 19 plots the computed drag coefficients versus Reynolds number and compares well to the results from Johnson and Patel [13] and experimental data from Roos and Willmarth [22]. The drag coefficient is computed as $C_D = F_x/\left(\frac{1}{2}\rho U_\infty^2 \pi D^2/4\right)$, where F_x is the force on the sphere in the streamwise direction. Figs. 20–23 depict the streamlines contours, vorticity contours, and three-dimensional particle path trace for $Re = 250$ corresponding to the steady non-axisymmetric flow regime for larger Reynolds number. These results are also in good agreement with results from Johnson and Patel [13].

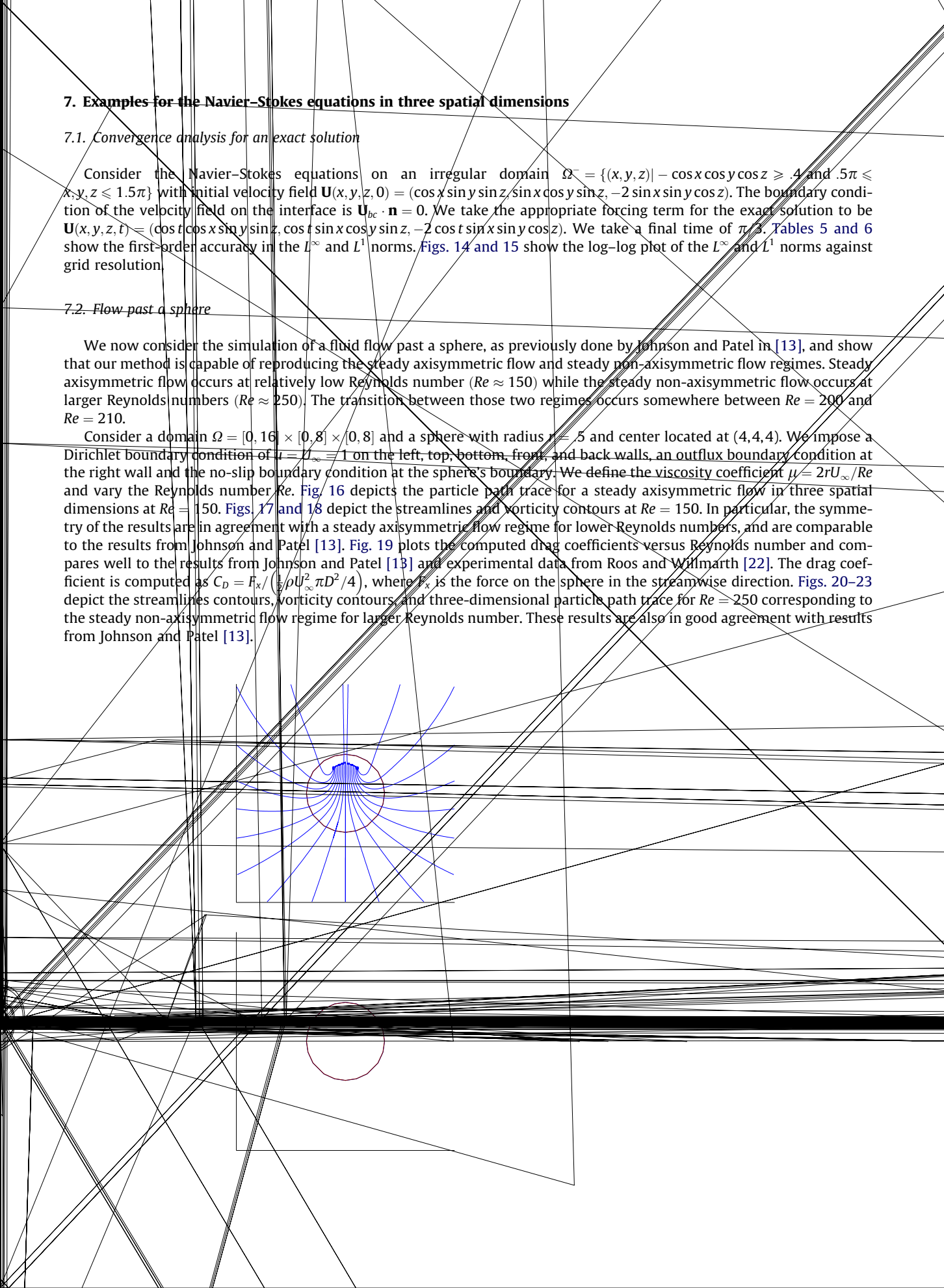

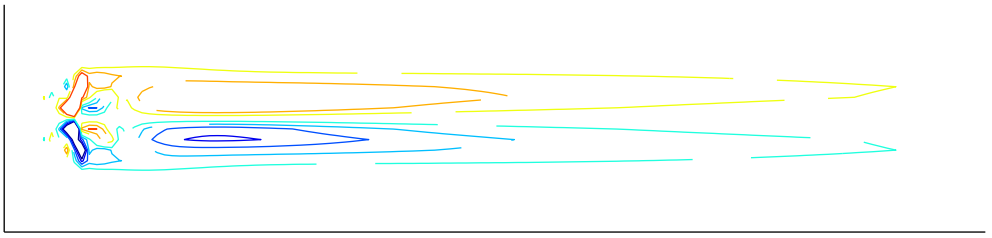

7.3. Ellipsoid rotating in closed box

Consider a domain $\Omega = [-1,1]^3$ and an ellipsoid with dimensions $radius_x = .5, radius_y = radius_z = .2$, centered at $(.2,0,0)$ at $t_n = 0$, and rotating around the pivot point $(0,0,0)$. We impose no-slip boundary conditions on all the domain walls and the

ellipsoid boundary. We define viscosity $\mu = .0001$ and angular velocity $\omega = .5$ in the clockwise direction around the z-axis. Figs. 24–26 depict the streamline slices and curl of velocity around the x-, y-, and z-axes. In Fig. 26, the streamlines and curl of velocity is symmetric on both sides of the $z = 0$ plane, since the rotation of the ellipsoid is around the z-axis only.

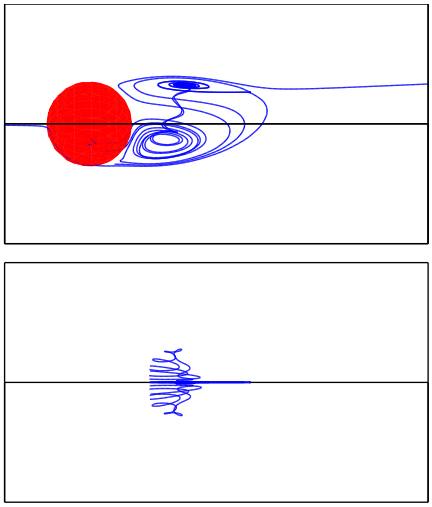

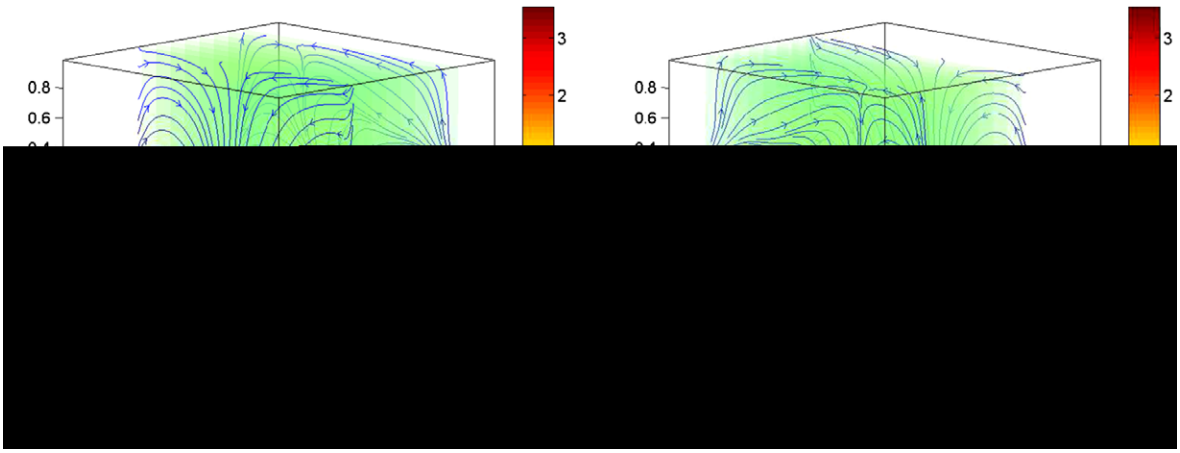

Fig. 25. Curl of velocity and streamlines around the y-axis, viewed down the positive y-axis (left) and negative y-axis (right), for example, Section 7.3.

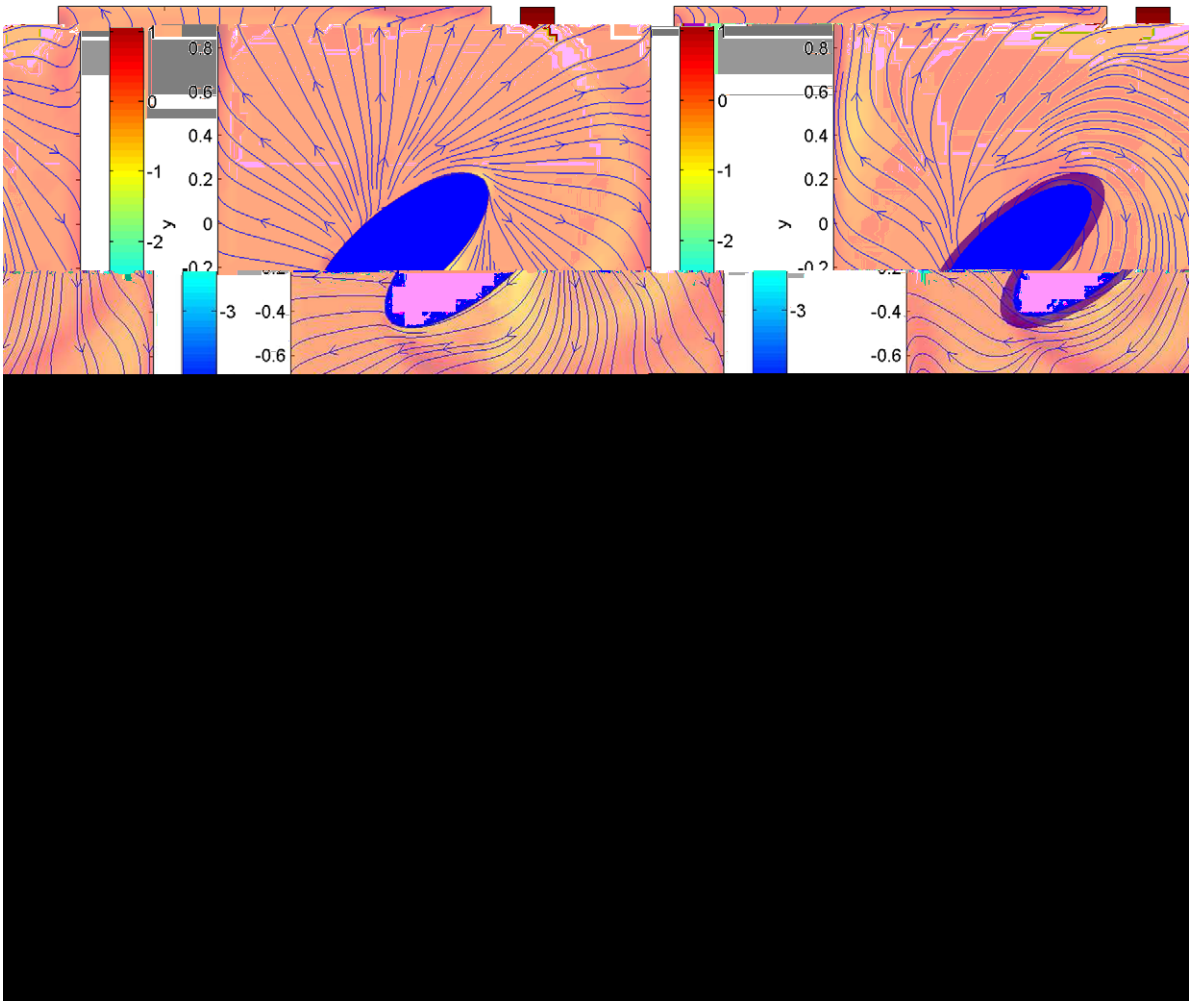

Fig. 26. Curl of velocity and streamlines around the z-axis, at slice $z = 0$ (top left), $z = \pm.1$ (top right), $z = \pm.2$ (bottom left), and $z = \pm.3$ (bottom right), for example, Section 7.3.

8. Conclusion

We have presented a novel and efficient discretization of the Navier–Stokes equations on irregular domains. The irregular domains can be of arbitrary shape and do not have to be approximated by domain rasterization. In particular, we have presented a novel discretization of the projection step that is straightforward to implement and leads to a symmetric positive definite linear system that can be inverted efficiently with standard methods. We demonstrated the second-order accuracy in two spatial dimensions and first-order accuracy in three spatial dimensions in the L^1 and L^∞ norms and we showed that this method can reproduce accurate fluid flow motions on irregular domains with examples in both two and three spatial dimensions.

Acknowledgments

The research of Y.T. Ng and F. Gibou were supported in part by a Sloan Research Fellowship in Mathematics, by the National Science Foundation under grant agreement DMS 0713858, by the Institute for Collaborative Biotechnologies through contract No. W911NF-09-D-0001 from the U.S. Army Research Office and by the Department of Energy under grant agreement DE-FG02-08ER15991. The research of C. Min was supported by the Korea Research Foundation Grant funded by the Korean Government (MOEHRD, Basic Research Promotion Fund) (KRF-2008-331-C00045).

References

[1] T. Aslam, A partial differential equation approach to multidimensional extrapolation, J. Comput. Phys. 193 (2004) 349–355.
[2] C. Batty, F. Bertails, R. Bridson, A fast variational framework for accurate solid–fluid coupling, in: ACM Trans. Graph. (SIGGRAPH Proc.), vol. 26(3), 2007.
[3] A. Belov, L. Martinelli, A. Jameson, A new implicit algorithm with multigrid for unsteady incompressible flow calculation, in: AIAA Paper 95-0049, 1995.
[4] M. Braza, P. Chassaing, H. Ha Minh, Numerical study and physical analysis of the pressure and velocity fields in the near wake of a circular cylinder, J. Fluid Mech. 165 (1986) 79–130.
[5] D. Calhoun, A cartesian grid method for solving the two-dimensional streamfunction-vorticity equations in irregular regions, J. Comput. Phys. 176 (2) (2002) 231–275.
[6] A. Chorin, A numerical method for solving incompressible viscous flow problems, J. Comput. Phys. 2 (1967) 12–26.
[7] M. Coutanceau, R. Bouard, Experimental determination of the main features of the viscous flow in the wake of a circular cylinder in uniform translation. Part 1. Steady flow, J. Fluid. Mech. 79 (1977) 231.
[8] S. Dennis, G. Chang, Numerical solutions for steady flow past a circular cylinder at Reynolds number up to 100, J. Fluid. Mech. 42 (1970) 471.
[9] F. Gibou, R. Fedkiw, L.-T. Cheng, M. Kang, A second-order-accurate symmetric discretization of the Poisson equation on irregular domains, J. Comput. Phys. 176 (2002) 205–227.
[10] C. Hirt, A. Amsden, J. Cook, An arbitrary Lagrangian–Eulerian computing method for all flow speeds, J. Comput. Phys. 135 (1974) 227–253.
[11] K. Ito, M.-C. Lai, Z. Li, A well-conditioned augmented system for solving Navier–Stokes equations in irregular domains, J. Comput. Phys. 228 (2009) 2616–2628.
[12] H. Johansen, P. Colella, A Cartesian grid embedded boundary method for Poisson's equation on irregular domains, J. Comput. Phys. 147 (1998) 60–85.
[13] T.A. Johnson, V.C. Patel, Flow past a sphere up to a reynolds number of 300, J. Fluid Mech. 378 (1999) 19–70.
[14] R. LeVeque, Z. Li, The immersed interface method for elliptic equations with discontinuous coefficients and singular sources, SIAM J. Numer. Anal. 31 (1994) 1019–1044.
[15] C. Liu, X. Zheng, C.H. Sung, Preconditioned multigrid methods for unsteady incompressible flows, J. Comput. Phys. 139 (1) (1998) 35–57.
[16] C. Min, F. Gibou, A second order accurate projection method for the incompressible Navier–Stokes equation on non-graded adaptive grids, J. Comput. Phys. 219 (2006) 912–929.
[17] C. Min, F. Gibou, Geometric integration over irregular domains with application to level set methods, J. Comput. Phys. 226 (2007) 1432–1443.
[18] C. Min, F. Gibou, A second order accurate level set method on non-graded adaptive Cartesian grids, J. Comput. Phys. 225 (2007) 300–321.
[19] C. Min, F. Gibou, H. Ceniceros, A supra-convergent finite difference scheme for the variable coefficient Poisson equation on non-graded grids, J. Comput. Phys. 218 (2006) 123–140.
[20] S. Osher, R. Fedkiw, Level Set Methods and Dynamic Implicit Surfaces, Springer-Verlag, New York, NY, 2002.
[21] C. Peskin, Flow patterns around heart valves: a numerical method, J. Comput. Phys. 10 (1972) 252–271.
[22] F.W. Roos, W.W. Willmarth, Some experimental results on sphere and disk drag, AIAA J. 9 (1971) 285–291.
[23] J.A. Sethian, Level Set Methods and Fast Marching Methods, Cambridge University Press, Cambridge, 1999.
[24] G.H. Shortley, R. Weller, The numerical solution of Laplaces equation, J. Appl. Phys. 9 (1938) 334–348.
[25] D. Xiu, G. Karniadakis, A semi-Lagrangian high-order method for Navier–Stokes equations, J. Comput. Phys 172 (2001) 658–684.